

Revealing the Effect of High Ni Content in Li-Rich Cathode Materials: Mitigating Voltage Decay or Increasing Intrinsic Reactivity

Xiaokang Ju, Xu Hou, Zhongqing Liu, Leilei Du, Li Zhang, Tangtang Xie, Elie Paillard, Taihong Wang, Martin Winter, and Jie Li*

Li-rich layered oxides are considered as one of the most promising cathode materials for secondary lithium batteries due to their high specific capacities, but the issue of continuous voltage decay during cycling hinders their market entry. Increasing the Ni content in Li-rich materials is assumed to be an effective way to address this issue and attracts recent research interests. However, a high Ni content may induce increased intrinsic reactivity of materials, resulting in severe side reactions with the electrolyte. Thus, a comprehensive study to differentiate the two effects of the Ni content on the cell performance with Li-rich cathode is carried out in this work. Herein, it is demonstrated that a properly dosed amount of Ni can effectively suppress the voltage decay in Li-rich cathodes, while over-loading of Ni, on the contrary, can cause structural instability, Ni dissolution, and nonuniform Li deposition during cycling as well as severe oxygen loss. This work offers a deep understanding on the impacts of Ni content in Li-rich materials, which can be a good guidance for the future design of such cathodes for high energy density lithium batteries.

intrinsic drawbacks, such as low initial Coulombic efficiency (CE) and inevitable voltage decay during cycling, which may lead to continuous loss of energy density and create difficulties for battery management system to monitor and control.^[6–11]

Numerous studies have focused on the mechanism and on mitigation strategies of voltage decay. Generally, the voltage decay is caused by many aspects, such as oxygen release, phase transition, and surface defects.^[12] When charging up to 4.5 V, the oxidation of O^{2-} to O_2 occurs to balance the delithiation from the Li_2MnO_3 phase, leading to the activation of the $Mn^{4+} \rightarrow Mn^{3+}$ reduction during discharge, which shows low redox potential.^[2] Therefore, the irreversible oxygen release occurring during prolonged cycles leads to severe voltage decay. Meanwhile, due to the bonds between transition metals (TMs)

and O get weakened by the formation of oxygen vacancies and the reduction of TM ions,^[13–15] TM easily migrates to Li layer sites, which can cause phase transition from layered structure to spinel phase (with the activation of Mn^{2+}/Mn^{3+} redox at 2.8 V vs Li/Li⁺), leading to a further decrease of average voltage.^[16,17] Except for the effect of structural change, extensive side reactions between activated oxygen species and the electrolyte also

1. Introduction

Because of the high specific capacities and low cost, lithium-rich layered nickel cobalt manganese oxides (LNCM) is considered as a promising and partially greener alternative to conventional cathodes for lithium rechargeable batteries.^[1–5] However, the practical application of them still suffers from

X. Ju, X. Hou, Z. Liu, M. Winter, J. Li
Helmholtz-Institute Muenster (HI MS), IEK-12
Forschungszentrum Juelich GmbH
Corrensstr. 46, 48149 Muenster, Germany

X. Ju, T. Wang
Pen-Tung Sah Institute of Micro-Nano Science and Technology
Xiamen University
No. 422, Siming South Road, Xiamen, Fujian 361005, China

 The ORCID identification number(s) for the author(s) of this article can be found under <https://doi.org/10.1002/smll.202207328>.

© 2023 The Authors. Small published by Wiley-VCH GmbH. This is an open access article under the terms of the Creative Commons Attribution-NonCommercial-NoDerivs License, which permits use and distribution in any medium, provided the original work is properly cited, the use is non-commercial and no modifications or adaptations are made.

L. Du, M. Winter
MEET Battery Research Center
Institute of Physical Chemistry
University of Muenster
Corrensstr. 46, 48149 Muenster, Germany

L. Zhang
Helmholtz Centre Berlin for Materials and Energy
Hahn-Meitner-Platz 1, 14109 Berlin, Germany

T. Xie, E. Paillard, J. Li
Department of Energy
Politecnico di Milano
Via Lambruschini, 4, Milano, MI 20156, Italy
E-mail: jie.li@polimi.it

T. Xie
The Testing and Technology Center for Industrial Products
Shenzhen Customs
Shenzhen, Guangdong 518067, China

DOI: 10.1002/smll.202207328

generate accumulated undesirable compounds on the electrode surface, which can increase cell impedance with the growth layer, leading to an increased overpotential.^[2] “substitution” of 3d TMs with larger 4d or 5d metal ions (e.g., Nb, Ru, Sn, and Ir) can suppress the voltage decay effectively by inhibiting the TMs migration to Li layers and thus stabilizing the oxygen redox, thus is the most widely used strategy to enhance the performance of LNCM cathodes.^[18–23] However, those alternative materials are hardly considered for practical application, since most of the used doping/substituting elements are rare and heavy.

An alternative procedure, i.e., adjusting the content of different TMs in LNCM, is proposed to be an economic way to address the issue of the voltage decay.^[24,25] It has been reported that when the Ni content increases, the formation of the layered Li₂MnO₃ component is suppressed, and subsequently lattice oxygen evolution can be reduced.^[26,27] In the meantime, nickel ions tend to reversibly migrate between the TM layer and the interlayer during the delithiation/lithiation process, which can suppress the formation of a spinel phase, leading to the improved cycle stability.^[27] However, in addition to a decrease in capacity, it brings new challenges in regard to higher surface reactivity with higher Ni content due to the raising risk of side reactions between Ni⁴⁺ and electrolytes. As being widely discussed in conventional high Ni layered cathodes, such as LiNi_{0.8}Co_{0.1}Mn_{0.1}O₂ (NCM811), the Ni⁴⁺ ions in delithiated materials are thermodynamically metastable against the typical organic carbonate electrolytes.^[28] Therefore, in addition to accelerating electrolyte decomposition, side reactions between Ni⁴⁺ and electrolyte also lead to the dissolution of Ni ions in the electrolyte upon intensive cycles. The dissolved Ni ions, together with dissolved Mn ions cause a distortion of the layered structure, and further aggravate oxygen evolution from the cathode. Besides, as being demonstrated in lithium metal batteries (LMBs), the dissolution of TM ions can affect the Li deposition behaviors and enlarge the overpotential on the anode. These problems should not be ignored when designing the high Ni LNCM cathodes.^[29] Hence, how to balance the TM ratio in LNCM to minimize the voltage decay and to realize high cycle stability becomes a critical concern in realizing the practical utilization of LNCM.

In this work, we aim to explore the effect of Ni content in LNCM materials on their structural stability, thermal stability, cathode/electrolyte interphase (CEI) formation, and Li deposition on Li metal anode by comparing three materials with different Ni content, i.e., 0.4Li₂MnO₃·0.6LiNi_{1/3}Co_{1/3}Mn_{1/3}O₂ (LNCM111), 0.4Li₂MnO₃·0.6LiNi_{0.6}Co_{0.2}Mn_{0.2}O₂ (LNCM622) and 0.4Li₂MnO₃·0.6LiNi_{0.8}Co_{0.1}Mn_{0.1}O₂ (LNCM811) (also written as Li_{1.16}Ni_{0.17}Co_{0.17}Mn_{0.50}O₂, Li_{1.16}Ni_{0.30}Co_{0.10}Mn_{0.44}O₂, and Li_{1.16}Ni_{0.40}Co_{0.05}Mn_{0.39}O₂, respectively). The investigation on the mutual restrictive effects of Ni and layered Li₂MnO₃ provides new insights into the optimization of TM ratio of LNCM to realize the balance of voltage decay and cycle stability.

2. Results and Discussions

2.1. Physical Properties and Electrochemical Performance of LNCM Materials

The chemical compositions of LNCM111, LNCM622, and LNCM811 were confirmed by Inductively Coupled Plasma

Emission Spectroscopy (ICP-OES), and the proportions of each metal element are listed in Table S1, Supporting Information. The results agree well with the designed contents of Li and TMs. Similar primary and secondary particle sizes of 100–300 nm and ≈4 μm, respectively, were gained for all three samples without obvious difference in particle shape, as displayed in Figure S1, Supporting Information. Therefore, any influence of particle morphology aspects^[3] on the electrochemical performance of LNCM materials can be eliminated during the following discussions.

The XRD patterns and related Rietveld refinement of LNCM materials are presented in Figure 1a–d. As shown in Figure 1a, each pattern exhibits the typical LiTMO₂ layered structure (*R* $\bar{3}m$) except reflections in the range of 20°–25° coming from Li₂MnO₃ (*C*2/m).^[26,30] Along with the increase of Ni content, the intensity of superstructure reflections drops, indicating a gradually decreased Li₂MnO₃ character. The proportions of Li₂MnO₃ component in LNCM111, LNCM622, and LNCM811 are about 38.0%, 23.6%, and 11.1%, respectively, as obtained from Rietveld refinement of XRD patterns (Figure 1b–d). The lattice parameter *a* and the unit cell volume *V* of the α-NaFeO₂ structure (Figure S2) increase with the Ni content, which accordingly originates from the decreased Mn⁴⁺ content in the particles as Mn⁴⁺ has a smaller ionic radius compared to other TM ions. The ratio of (003) and (104) peak intensity (*I*₀₀₃/*I*₁₀₄) are 2.0, 1.6, and 1.2 for LNCM111, LNCM622, and LNCM811, respectively, indicating high cation mixing in LNCM811 sample.^[31,32]

Raman spectroscopy of LNCM materials was measured to study the crystal structure evolution, since the vibration of TM–O is sensitive in transition-metal oxides (Figure 1e). Two broad bands at 400 cm^{−1} (*E*_g) and 600 (*A*_{1g}) cm^{−1}, corresponding to the typical layered α-NaFeO₂ structure with *R* $\bar{3}m$ space group, are observed in all three LNCM samples. Both peaks show a slightly red shift with the Ni content increase, which is similar to the trend of the results from commercialized LiTMO₂ samples (Figure S3, Supporting Information). Meanwhile, the bands below 430 cm^{−1} that are assigned to the Li₂MnO₃ component,^[33] gradually decrease with increase of Ni content, suggesting that the high Ni content can suppress the formation of Li₂MnO₃ component, which is consistent with XRD refinement results. Consequently, in order to maintain the electro-neutrality, the average valence state of Ni increases in the LNCM samples with high Ni content, which is confirmed by the Ni K-edge change in XANES (Figure 1f) and Ni 2p spectra in X-ray photoelectron spectroscopy (XPS) measurement (Figure S4, Supporting Information). In the meantime, the valences of Co and Mn remain at +3 and +4, respectively, for all three samples regardless of TM ratio variation (Figure S5, Supporting Information), which is consistent with previous reports.^[26,34]

Initial charge–discharge profiles and corresponding differential capacity (dQ/dV) vs voltage plots of lithium metal cells with LNCM111, LNCM622, and LNCM811 cathodes are shown in Figure 2a and Figure S6, Supporting Information, respectively. All cells were cycled in two-electrode 2032-coin cells with Li metal as anode between 2.0 and 4.8 V at 0.1 C (1 C = 250 mA g^{−1}). Upon 4.45 V during charge, the region which is ascribed to the oxidation of TM (mainly Ni) in LiTMO₂,^[35] prolongs from LNCM111 to LNCM811 due to the increase of the LiTMO₂ component, as confirmed by XRD refinement. On the contrary, the plateau above 4.45 V, which mainly refers to the O^{2−} oxidation

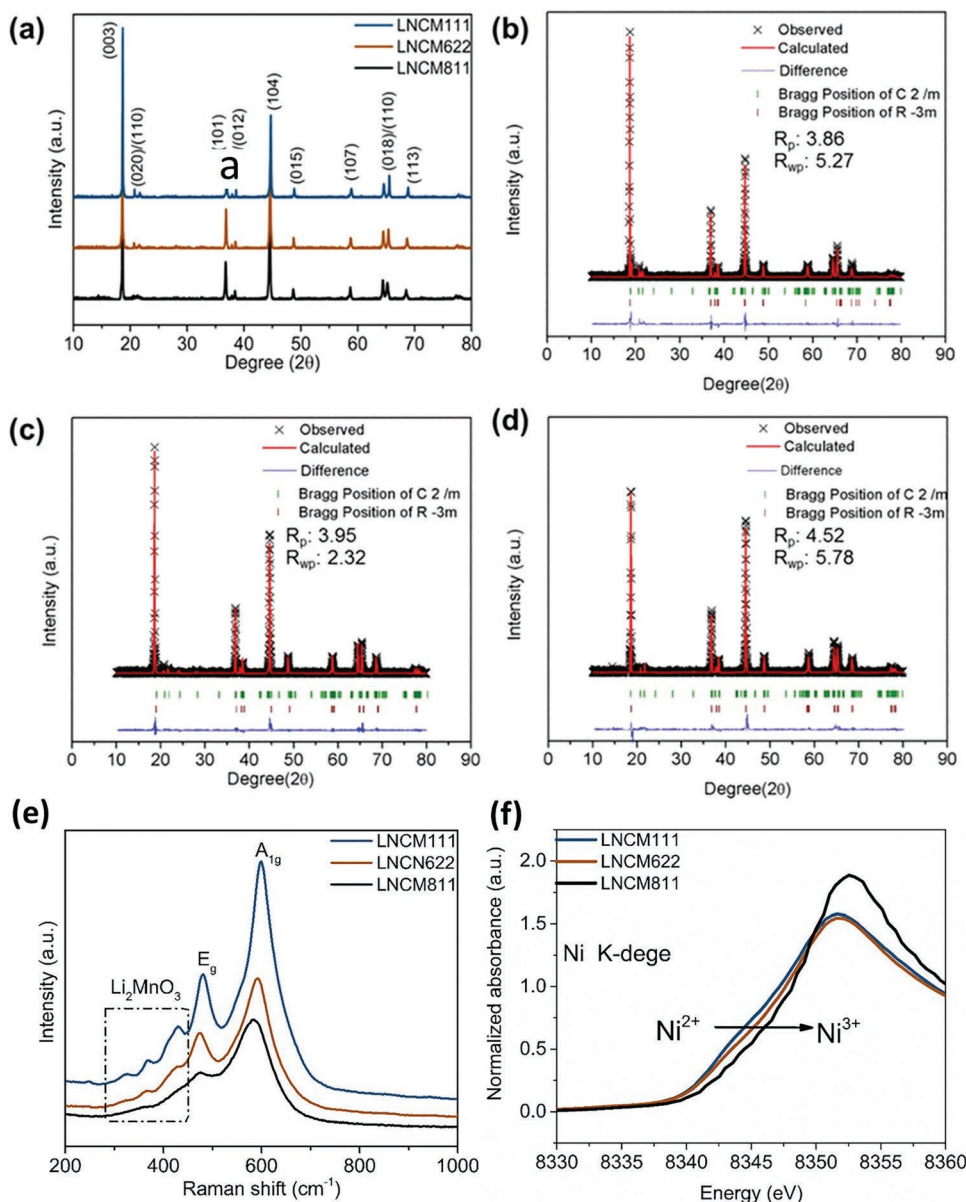


Figure 1. a) XRD patterns of the three samples; b–d) Rietveld refinement patterns, e) Raman spectra, and f) Ni K-edge XANES spectra of LNCM111, LNCM622, and LNCM811, respectively.

in Li_2MnO_3 , shortens along with the Ni content increase owing to the suppressed Li_2MnO_3 component.^[26] Thus, higher Ni content results in lower contribution of oxygen redox, leading to lower discharge capacity, e.g., the initial discharge capacities at 0.1 C are 267, 255, and 222 mAh g^{-1} for LNCM111, LNCM622, and LNCM811, respectively.

The mean discharge voltages of the three LNCM cathodes during cycling are shown in Figure 2b. The cells were cycled at 0.5 C after two formation cycles at 0.1 C at the range of 2.0–4.8 V. Although LNCM811 possesses the highest mean discharge voltage in the first formation cycle, and it drops in the subsequent cycles. The voltage decay per cycle is 1.62, 1.06, and 1.33 mV (vs the 1st value at 0.5 C within 100 cycles) for LNCM111, LNCM622, and LNCM811, respectively. Obviously, increasing Ni content in LNCM materials leads to less voltage

decay, but overloading of the Ni content can undesirably aggravate this issue. The intrinsic instability of Ni^{4+} at highly delithiated states (e.g., at 4.8 V) is expected to be the main reason, together with the weakened role of Li_2MnO_3 in stabilizing the layered structure.^[9] The cycling performance of the three LNCM materials is shown in Figure 2c. Though LNCM111 delivers the highest initial discharge capacity, it experiences a relatively serious capacity fading during the long-term cycling in comparison with that of the other two samples. No capacity fading is seen from LNCM622, and the discharge capacity even shows a slight increase in the first 50 cycles, which agrees with the previous report from Manthiram et al.^[26] LNCM622 overtakes LNCM111 at the 28th cycle and further widens the gap during the following cycles. Besides, LNCM622 exhibits the most stable Coulombic efficiency than the other two samples (Figure S7,

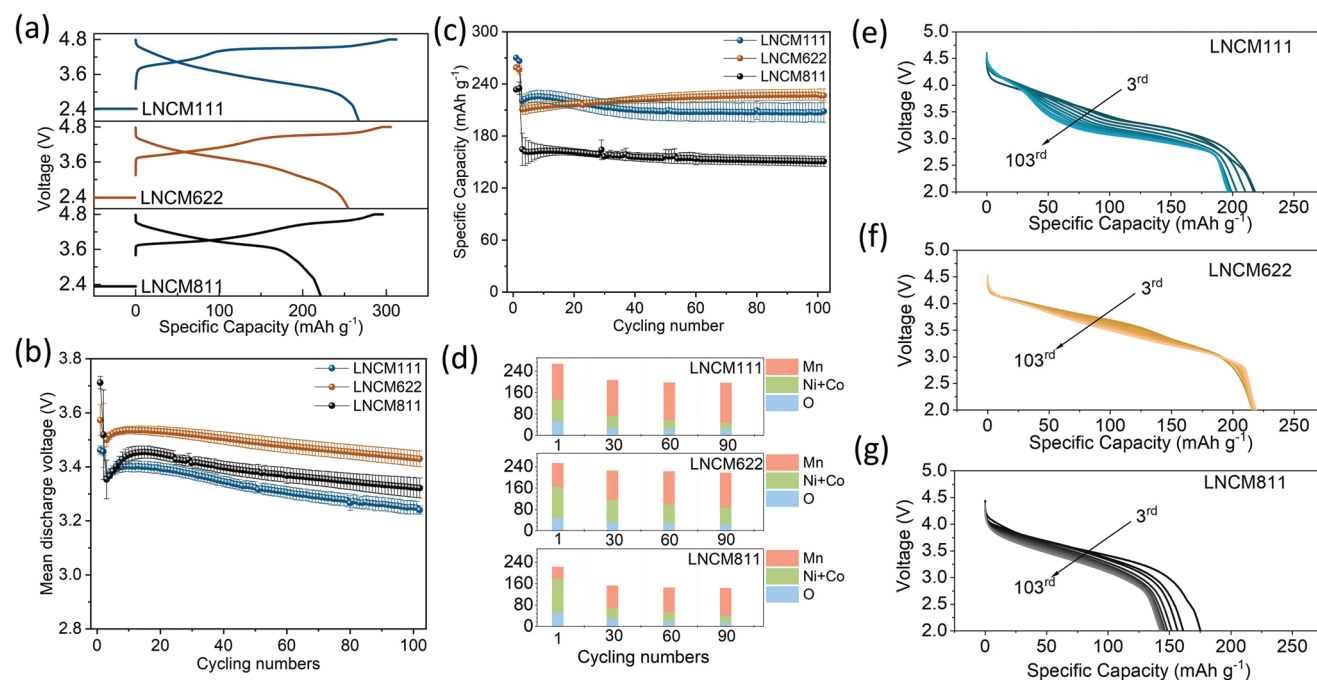


Figure 2. a) Initial charge–discharge curves of Li metal cells with three LNCM electrodes at 0.1 C. b) Mean discharge voltage and c) cycling performance of three LNCM electrodes when being investigated at 0.1 C for two formation cycles and at 0.5 C for the following cycles. d) Respective contributions of TMs and O on the capacity in LNCM111, LNCM622, and LNCM811 at various cycles. Discharge curves of Li metal cells recorded per 10 cycles with e) LNCM111, f) LNCM622, and g) LNCM811 electrodes within 100 cycles at 0.5 C.

Supporting Information). For LNCM811, it shows a notably low capacity, which is less interesting for Li-rich materials. Even if prolonged to 200 cycles, as shown in Figure S8, Supporting Information, LNCM622 still exhibits superior electrochemical performances with no capacity fading and good rate capability. Hence optimization Ni content in Li-rich cathodes, e.g. that of LNCM622, can not only suppresses the voltage decay, but also maintains a desirable capacity.

To further understand the role of each element in charge compensation and the evolution of redox couples during cycling, the contributions of TMs and O on the discharge capacity in LNCM111, LNCM622, and LNCM811 are compared in Figure 2d. Specifically, three regions are divided according to the redox potential peaks shown in dQ/dV plots (Figure S6, Supporting Information), namely, oxygen reduction (above ≈ 4.2 V vs $\text{Li}|\text{Li}^+$), the reduction of $\text{Ni}^{4+}/\text{Ni}^{3+}/\text{Ni}^{2+}$ and $\text{Co}^{3.6+}/\text{Co}^{3+}$ (≈ 3.4 – 4.2 V vs $\text{Li}|\text{Li}^+$), and reduction of Mn (below ≈ 3.4 V vs $\text{Li}|\text{Li}^+$).^[14,24] Regarding LNCM111, along cycling, the participation of oxygen, Ni, and Co redox to the total specific capacity notably decrease, and the contribution of Mn redox steadily increases. In comparison, the increase of Mn redox contribution is slower and a proportion from Ni and Co redox maintains higher values in LNCM622. When Ni content further increases, a high capacity of 146 mAh g^{-1} in the initial discharge contributed by Ni and Co redox is delivered in LNCM811. As most of the Ni ions are gradually deactivated during the following cycles, the capacity delivered by Ni and Co redox in the 90th cycle is only 36 mAh g^{-1} . Therefore, further increasing the Ni content promotes negative effects on performance at high voltage.

The effect of Ni content on the Li^+ diffusion kinetics was detected by EIS measurements on cells at the first discharge

at 2.0 V. The fitted results and the equivalent circuit used are shown in Figure S9. The charge transfer resistance (R_{ct}) of LNCM111, LNCM622, and LNCM811 is 54.2, 43.9, and 90.3 Ω , respectively. LNCM622 shows the lowest R_{ct} among the three samples.^[36] Since Li_2MnO_3 has poor ionic conductivity, the suppressed Li_2MnO_3 component in LNCM622 results in a reduced R_{ct} compared to LNCM111. However, severe side reaction between Ni and electrolyte at high charge voltage causes an increase of impedance again. Even the content of the Li_2MnO_3 component decreases in LNCM811. Figure 2e–g presents the discharge voltage profiles within 100 cycles recorded per 10 cycles, facilitating the comparison of capacity and voltage degradation. Obviously, LNCM111 and LNCM811 with either high Mn or Ni content both exhibit serious voltage decay, while LNCM622 with a proper Ni content shows much better maintenance of voltage.

2.2. The Effect of Ni Content on Structural Stability During Cycling

To investigate the structural stability of materials during cycling, Raman spectroscopy was performed on electrodes cycled at 0.5 C for 100 cycles (Figure 3a). Compared with the pristine materials (Figure 1e), a new peak appears in each spectrum at around 640 cm^{-1} , which is assigned to A_{1g} vibration band of the spinel phase. The peak intensity is higher in the spectrum of cycled LNCM111 electrode than the other two samples, indicating that LNCM111 undergoes the most pronounced structural change during cycling. In other words, this observation indicates that an increasing Ni content inhibits the phase

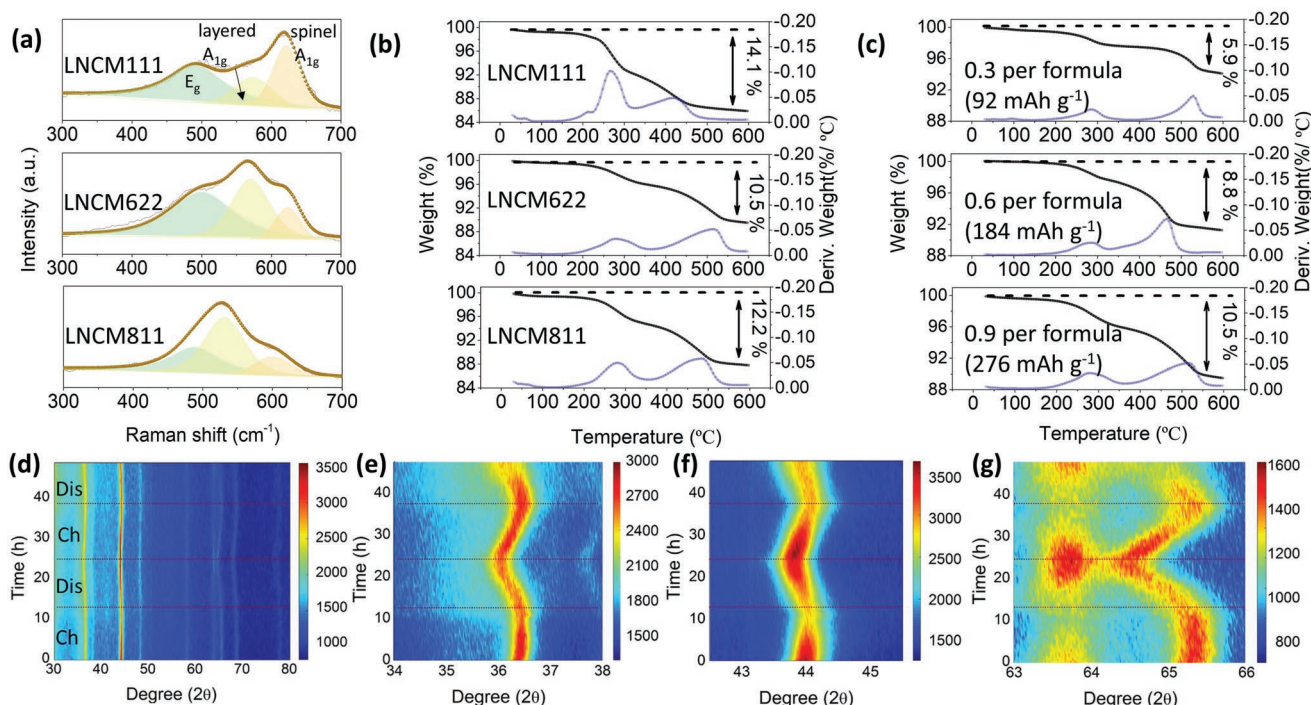


Figure 3. a) Raman spectra of LNCM111, LNCM622, and LNCM811 electrodes after cycling; b) TGA curves and corresponding differential points (blue line) of all three samples with a delithiated amount of 0.9 per formula; c) TGA and corresponding differential curves (blue line) of LNCM622 at various delithiated amounts; d) waterfall plot of in situ XRD pattern for LNCM622 cathode during the first two cycles at 0.1 C with 2θ range of 30° – 80° and corresponding magnified patterns of e) (101) peak; f) (104) peak; g) (018) and (110) peaks.

transition of LNCM from layered to spinel. However, though less phase transition occurs in the cycled LNCM811 electrode, the peak positions of A_{1g} shift to the left obviously, which is ascribed to the Ni ions in high valence, demonstrating the loss of Ni ions redox activity in LNCM811 when being cycled at high cutoff voltage and the maintenance of Ni ion at a high oxidation state at the discharged state.^[37–39] Therefore, the Ni content should be strictly controlled when designing LNCM materials, and the previous statement^[10,34] that increasing the Ni content can suppress the voltage decay of LNCM is only applicable under certain limitation.

As oxygen loss at high voltage during the cycling can directly reflect on the voltage decay of LNCM materials, investigations on oxygen activity as well as structural evolution at highly delithiated states is important. To achieve this target effectively, chemical delithiation process (with NO_2BF_4) was used to obtain “clean” delithiated samples in this work,^[40] in order to avoid the influence of PVdF and conductive carbon which would residue in electrochemical delithiated electrodes. The delithiation amount is fixed to 0.9 per formula, corresponding to a charge capacity of 276 mAh g^{-1} based on LNCM622. Figure 3b shows the TGA curves and corresponding differential curves of all chemically delithiated samples. Within 30 – 600°C , the weight losses of LNCM111, LNCM622, and LNCM811 are 14.1%, 10.5%, and 12.2%, respectively. Since the weight loss mainly comes from oxygen release^[41] in this case, the LNCM622 sample clearly shows the least oxygen loss and the best thermodynamic stability at high delithiated condition. The oxygen release from LNCM622 at different delithiated states, i.e., 0.3, 0.6, and 0.9 per formula (corresponding to a capacity of 92, 184 and

276 mAh g^{-1} , respectively), was further explored, and the results are displayed in Figure 3c. With the increase of delithiation amount, the oxygen loss increases gradually, this would lead to the structural rearrangement^[40,42] and therefore result in the degradation of electrochemical performance of LNCM materials.

Figure 3d and Figure S10, Supporting Information show the contour map and waterfall plots of in situ XRD patterns for the LNCM622 electrode during the first two cycles in the 2θ range of 30° – 80° , respectively. The magnified maps on (101), (104), (018), and (110) peaks are shown in Figure 3e–g. During the initial charge-discharge process, due to the irreversible removal of Li^+ and oxygen from the lattice, the (101) and (110) peaks could not return to the original positions and slightly shift to the left with shorten lattice spacing. However, during the second cycle, the reversibility of the structural change increases, and the peak positions move back to those at end of the first discharge without obvious change. Besides, no new peak appears during this process, demonstrating a single-phase reaction. Therefore, LNCM622 shows high structural stability, which is consistent with the results of Raman and TGA measurements.

2.3. The Effect of Ni Content on Side Reaction between Electrode and Electrolyte

The side reaction between high valence Ni and electrolyte is leading to the degradation of LNCM materials due to thick CEI formation during cycling. Here, XPS was used to clarify the components and thickness of CEI and investigate the interactions between electrode and electrolyte.^[43,44] Figure 4a–d shows

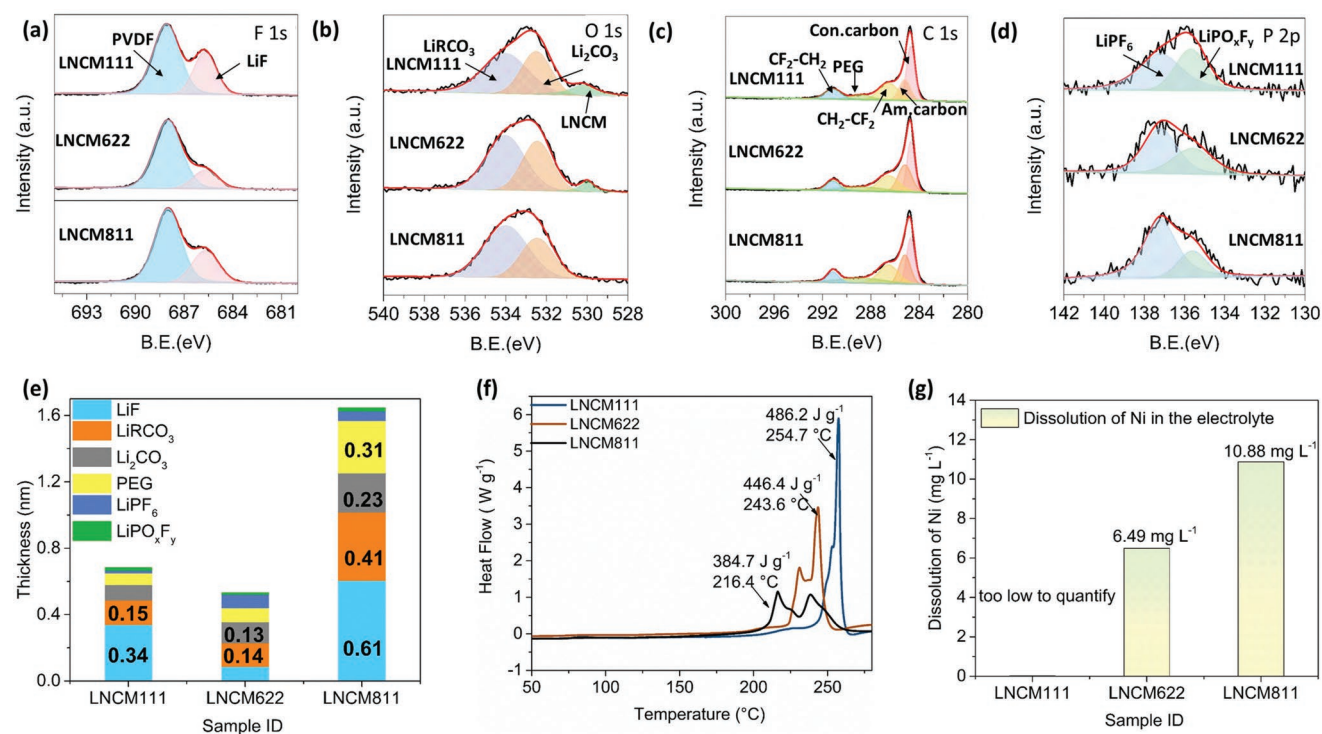


Figure 4. a) F 1s, b) O 1s, c) C 1s, and d) P 2p XPS spectra of LNCM111, LNCM622, and LNCM811 electrodes after 5 cycles; e) quantification of the thickness contribution from each component in the CEI for different LNCM electrodes; f) DSC curves of LNCM electrodes after charging to 4.8 V, the measurement was carried out with LP57 electrolyte; g) dissolution of Ni in LP57 electrolyte of three LNCM electrodes after 5 cycles.

the F 1s, O 1s, C 1s and P 2p spectra of LNCM111, LNCM622 and LNCM811 electrodes after 5 cycles at 0.1 C. In F 1s spectra (Figure 4a), two peaks at 688.1 and 686.7 eV are detected, which can be assigned to PVdF^[45] and LiF,^[46] respectively. The peak from O 1s spectra (Figure 4b) at 534.0 and 532.5 eV are assigned to organic carbonate compounds (LiRCO₃) and Li₂CO₃, respectively, which are considered as the main components of CEI layer. Besides, the peak at 528.3 eV corresponds to the LNCM active material.^[44] It disappears on the surface of cycled LNCM811 electrode, indicating that its CEI layer constructed by products from side reactions and decompositions of electrolytes is much thicker than that of the other two electrodes. The C 1s spectra can be fitted with five peaks corresponding to CF₂-CH₂, polyethylene glycol (PEG), CH₂-CF₂, porous carbon, and conductive carbon with the binding energy from high to low.^[47] Two peaks can be identified in P 2p spectra, i.e., LiPF₆ at a higher binding energy (139.2 eV) and LiPO_xF_y at a lower binding energy (135.7 eV). Therefore, the CEI layer is composed of LiF, LiRCO₂, Li₂CO₃, PEG, LiPF₆, etc., which is consistent with previous literature.^[48,49] Using the previously reported CEI calculation formula,^[46,50,51] the CEI thicknesses of LNCM111, LNCM622, and LNCM811 are calculated to be 0.68, 0.53, and 1.65 nm, respectively, based on the intensity of Mn 2p signal of cycled electrodes (Figure S11, Supporting Information). The contents of individual CEI ingredients for three electrodes are further quantitative calculated, as shown in Figure 4e. The LNCM811 electrode has the thickest CEI, dominated by LiF and LiRCO₃, indicating more electrolyte consumption and unfavorable side effects during the cycling, as well as the increased interfacial impedance in the cell.

As reported, the highly delithiated layered cathodes show high reactivity with the organic solvent-based electrolyte at elevated temperature, leading to a thermal run-away.^[40] Figure 4f shows the DSC curves of electrodes directly disassembled from coin cells after the first charge step (to 4.8 V). Within 50–280 °C, the main exothermic peak shifts toward low temperature, and the released heat gradually decreases along with the increase of Ni content. For example, in LNCM111, the main exothermic peak is located at 254.7 °C, and the released heat is 486.2 J g⁻¹. While, LNCM811 starts to decompose at 216.4 °C and generate 384.7 J g⁻¹ heat upon heating. It indicates that the lower thermal run-away temperature occurs for samples with higher nickel content. Since both lower reaction temperature and higher exothermic heat cause safety issues, adjusting the TM ratio appropriately is important to enhance the intrinsic safety of materials.

The side reactions between the electrode and electrolyte also cause the dissolution of metal ions in electrolyte, which can result in capacity fading as well. Thus, to determine the amounts of dissolved TMs, the electrolytes collected from the cells after 5 cycles were measured with ICP-OES (Figure 4g). No signals from Mn and Co have been detected in this experiment, probably due to the reason that Mn precipitates on the anode and Co is much more stable to stay on the crystal sites.^[52,53] Nevertheless, LNCM811 shows the highest value of Ni dissolution (10.88 mg L⁻¹), clearly due to the severe side reactions originated by the high Ni content. This result further illustrates the importance of regulating the TM ratio to achieve high thermal stability. Side reactions between Ni and the electrolyte should be considered in designing Li-rich material despite of the positive role of Ni in this system.

2.4. The Effect of Ni Content on the Lithium Deposition/Dissolution Processes

It has been demonstrated that the dissolved *TMs* can affect Li deposition/dissolution on the Li metal anode in LMBs even during the first Li deposition process.^[52] Thus, as clarified by ICP-OES results (Figure 4g), i.e., the different Ni content results in different *TM* dissolution behavior, the influence of Ni content in LNCM on the Li deposition performance is critical to be investigated. Meanwhile, the initial Li deposition morphology during the first charge process plays a crucial role on the cycle stability in LMBs.^[54–56] *TM* deposition along with Li deposition can cause an uneven deposition of Li metal with massive sizes and morphologies.^[57] In fact, deposited Li with high-surface-area is not favorable in particular lithium dendrite and “dead Li” formation.^[58]

Figure 5a–c shows the SEM images of Li deposition on Cu substrate for 15 h at a current density of 0.1 C (0.15 mA cm⁻²). The surface morphology of the Cu foil substrate is shown in Figure S12, Supporting Information, and the mass loading of cathode materials in this experiment is about 7 mg cm⁻². After Li deposition, the Cu surface is covered by aggregated “nodule-like” and “rod-like” Li depositions, which is consistent with the previous report.^[59] By comparison, it is clear that dense deposition occurs on Li surface with LNCM622 cathode, which may be caused by the suppressed *TM* dissolution in LNCM622. Therefore, the mild *TMs* dissolution is favorable for Li uniform deposition.

Furthermore, the initial potential profiles of Li metal anode with various cathodes at 0.1 C were obtained via measurement

of three-electrode Swagelok cells (Figure 5d). Li potential profiles can be distinguished into three parts (represented as I, II, and III).^[58] Before electrochemical reactions, due to the contact between electrolyte and Li metal, a passivation layer called solid electrolyte interphase (SEI) is formed at the Li anode surface. The first charge step (Process I) is accompanied by a sudden spike in potential, which is highly associated with experimental conditions, including current density, electrolyte formulation, type of cathode, thickness of the formed SEI, etc. The fragile SEI film cracks because of the stress change caused by Li deposition, which can facilitate Li deposition on the surface of Li metal. As a result, both the interphasial impedance and the overpotential of the lithium metal anode decrease (process II). In the subsequent discharge process, the previously deposited Li does preferentially dissolve, and this process is accompanied by a new SEI re-formation (process III). Since the surface of the Li anode is covered with SEI layer, leading to an overpotential increase, the kinetics of Li deposition/dissolution on the anode can be directly compared by the different overpotentials. Figure 5d clearly demonstrates that during the initial cycle, the cell with the LNCM622 cathode exhibits the lowest overpotential among the three cells, indicating a facilitated lithium deposition/dissolution behavior. This advantage can be maintained during extended cycling, as can be seen in Figure S13, Supporting Information. Therefore, Li deposition/dissolution process needs to be carefully considered for evaluating the performance of LNCM. Ni content actually plays an important role in the amount of dissolved *TM* ion as well as in Li anode deposition/dissolution behavior in the presence of LNCM cathode materials.

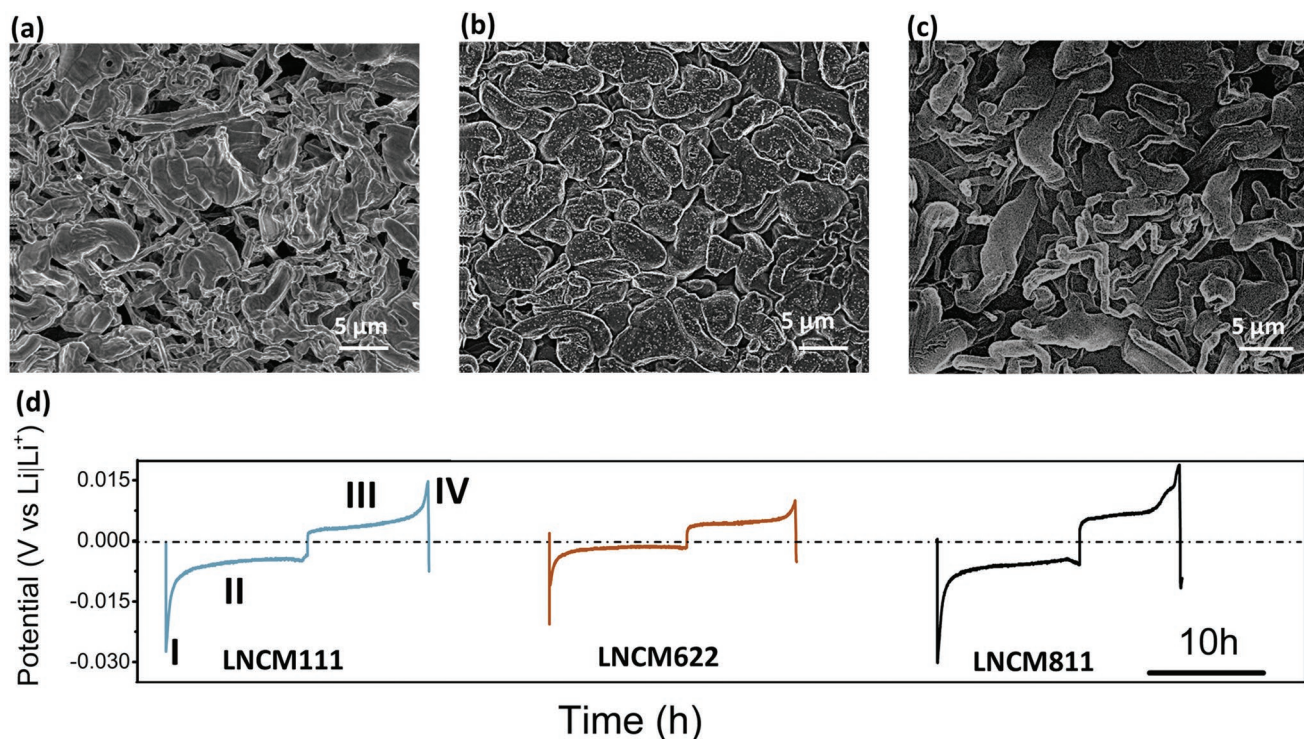


Figure 5. SEM images of Li deposits on Cu foil after the first lithium deposition at 0.1 C with a) LNCM111, b) LNCM622, and c) LNCM811; d) overpotential profiles at the first cycle for Li anodes in various cathodes.

3. Conclusion

In this work, we evaluated the effects of Ni content in Li-rich layered cathodes (LNCM) on various material and cell properties, such as structural stability, thermal stability, CEI formation, TM dissolution, and Li deposition during cycling. In difference to previous results that an increase of the Ni content can suppress the voltage fade in LNCM., we demonstrate that the intrinsic reactivity of Ni⁴⁺ in LNCM with high Ni content aggravates voltage decay and capacity fading due to the severe side reaction with the electrolyte, in particular Ni dissolution. Hence, Ni can only take over the desired beneficial role in mitigating voltage decay with a suitable TM ratio. The voltage decay associated with oxygen loss is serious, at either high Ni or Mn contents in LNCM materials. In addition, through the intensive studies on the thickness and chemical composition of CEI, the dissolution of TMs into the electrolyte, and the heat, we also indicate the strong correlation between the TM ratio in cathodes and the side reactions between cathode and electrolyte. Furthermore, nonuniform Li deposition and large overpotentials were observed in lithium metal cells using LNCMs with high Ni content. In a word, a suitable TM ratio, especially proper Ni content, for LNCM (e.g., LNCM622) could not only alleviate voltage decay, but also provide better compatibility with the electrolyte and the Li metal anode. These results are essential for adequately utilizing high-capacity lithium-rich cathodes in the future.

Supporting Information

Supporting Information is available from the Wiley Online Library or from the author.

Acknowledgements

X.J., and X.H. contributed equally to this work. The authors kindly acknowledge China Scholarship Council (CSC) and German Research Foundation (DFG, project Li 2916/2-1) for the funding support. [Correction added after publication 17 May 2023: Affiliations were corrected.]

Open Access Funding provided by Politecnico di Milano within the CRUI-CARE Agreement.

Conflict of Interest

The authors declare no conflict of interest.

Data Availability Statement

The data that support the findings of this study are available from the corresponding author upon reasonable request.

Keywords

cycle stability, high Ni content, Li-rich cathodes, mitigating voltage decay, oxygen loss

Received: November 24, 2022

Revised: January 9, 2023

Published online: February 17, 2023

- [1] H. Yu, H. Zhou, *J. Phys. Chem. Lett.* **2013**, *4*, 1268.
- [2] E. Hu, X. Yu, R. Lin, X. Bi, J. Lu, S. Bak, K.-W. Nam, H. L. Xin, C. Jaye, D. A. Fischer, *Nat. Energy* **2018**, *3*, 690.
- [3] X. He, J. Wang, R. Wang, B. Qiu, H. Frielinghaus, P. Niehoff, H. Liu, M. C. Stan, E. Paillard, M. Winter, *J. Mater. Chem. A* **2016**, *4*, 7230.
- [4] W. He, F. Ye, J. Lin, Q. Wang, Q. Xie, F. Pei, C. Zhang, P. Liu, X. Li, L. Wang, B. Qu, D.-L. Peng, *Nano-Micro Lett.* **2021**, *13*, 205.
- [5] Y.-L. Heng, Z.-Y. Gu, J.-Z. Guo, X.-T. Wang, X.-X. Zhao, X.-L. Wu, *Energy Mater.* **2022**, *2*, 200017.
- [6] P. K. Nayak, E. M. Erickson, F. Schipper, T. R. Penki, N. Munichandraiah, P. Adelhelm, H. Sclar, F. Amalraj, B. Markovsky, D. Aurbach, *Adv. Energy Mater.* **2018**, *8*, 1702397.
- [7] H. Guo, Z. Wei, K. Jia, B. Qiu, C. Yin, F. Meng, Q. Zhang, L. Gu, S. Han, Y. Liu, H. Zhao, W. Jiang, H. Cui, Y. Xia, Z. Liu, *Energy Storage Mater.* **2019**, *16*, 220.
- [8] J.-L. Shi, D.-D. Xiao, M. Ge, X. Yu, Y. Chu, X. Huang, X.-D. Zhang, Y.-X. Yin, X.-Q. Yang, Y.-G. Guo, L. Gu, L.-J. Wan, *Adv. Mater.* **2018**, *30*, 1705575.
- [9] M. M. Thackeray, S.-H. Kang, C. S. Johnson, J. T. Vaughey, R. Benedek, S. A. Hackney, *J. Mater. Chem.* **2007**, *17*, 3112.
- [10] X.-D. Zhang, J.-L. Shi, J.-Y. Liang, Y.-X. Yin, J.-N. Zhang, X.-Q. Yu, Y.-G. Guo, *Adv. Mater.* **2018**, *30*, 1801751.
- [11] Y. Zuo, B. Li, N. Jiang, W. Chu, H. Zhang, R. Zou, D. Xia, *Adv. Mater.* **2018**, *30*, 1707255.
- [12] W. He, W. Guo, H. Wu, L. Lin, Q. Liu, X. Han, Q. Xie, P. Liu, H. Zheng, L. Wang, X. Yu, D.-L. Peng, *Adv. Mater.* **2021**, *33*, 2005937.
- [13] J. R. Croy, M. Balasubramanian, K. G. Gallagher, A. K. Burrell, *Acc. Chem. Res.* **2015**, *48*, 2813.
- [14] J. R. Croy, D. Kim, M. Balasubramanian, K. Gallagher, S.-H. Kang, M. M. Thackeray, *J. Electrochem. Soc.* **2012**, *159*, A781.
- [15] J. R. Croy, K. G. Gallagher, M. Balasubramanian, Z. Chen, Y. Ren, D. Kim, S.-H. Kang, D. W. Dees, M. M. Thackeray, *J. Phys. Chem. C* **2013**, *117*, 6525.
- [16] T. Liu, A. Dai, J. Lu, Y. Yuan, Y. Xiao, L. Yu, M. Li, J. Gim, L. Ma, J. Liu, *Nat. Commun.* **2019**, *10*, 4721.
- [17] D. Kim, G. Sandi, J. R. Croy, K. G. Gallagher, S.-H. Kang, E. Lee, M. D. Slater, C. S. Johnson, M. M. Thackeray, *J. Electrochem. Soc.* **2012**, *160*, A31.
- [18] Q. Li, D. Zhou, L. Zhang, D. Ning, Z. Chen, Z. Xu, R. Gao, X. Liu, D. Xie, G. Schumacher, *Adv. Funct. Mater.* **2019**, *29*, 1806706.
- [19] J. Lee, D.-H. Seo, M. Balasubramanian, N. Twu, X. Li, G. Ceder, *Energy Environ. Sci.* **2015**, *8*, 3255.
- [20] K. Dai, J. Wu, Z. Zhuo, Q. Li, S. Sallis, J. Mao, G. Ai, C. Sun, Z. Li, W. E. Gent, *Joule* **2019**, *3*, 518.
- [21] J. C. Knight, P. Nandakumar, W. H. Kan, A. Manthiram, *J. Mater. Chem. A* **2015**, *3*, 2006.
- [22] Y. Miura, Y. Yasui, M. Sato, N. Igawa, K. Kakurai, *J. Phys. Soc. Jpn.* **2007**, *76*, 033705.
- [23] A. J. Perez, Q. Jacquet, D. Batuk, A. Iadecola, M. Saubanère, G. Rousse, D. Larcher, H. Vezin, M.-L. Doublet, J.-M. Tarascon, *Nat. Energy* **2017**, *2*, 954.
- [24] S. Shen, Y. Hong, F. Zhu, Z. Cao, Y. Li, F. Ke, J. Fan, L. Zhou, L. Wu, P. Dai, *ACS Appl. Mater. Interfaces* **2018**, *10*, 12666.
- [25] C. Jiao, G. Xu, M. Wang, Y. Zhao, B. Huang, *Solid State Ionics* **2021**, *369*, 115722.
- [26] J. C. Knight, A. Manthiram, *J. Mater. Chem. A* **2015**, *3*, 22199.
- [27] J.-L. Shi, J.-N. Zhang, M. He, X.-D. Zhang, Y.-X. Yin, H. Li, Y.-G. Guo, L. Gu, L.-J. Wan, *ACS Appl. Mater. Interfaces* **2016**, *8*, 20138.
- [28] I. Cekic-Laskovic, N. von Aspern, L. Imholt, S. Kaymaksiz, K. Oldiges, B. R. Rad, M. Winter, *Electrochem. Energy Storage* **2019**, https://doi.org/10.1007/978-3-030-26130-6_1.
- [29] W. Zuo, M. Luo, X. Liu, J. Wu, H. Liu, J. Li, M. Winter, R. Fu, W. Yang, Y. Yang, *Energy Environ. Sci.* **2020**, *13*, 4450.

- [30] N. Yabuuchi, M. Takeuchi, M. Nakayama, H. Shiiba, M. Ogawa, K. Nakayama, T. Ohta, D. Endo, T. Ozaki, T. Inamasu, *Proc Natl Acad Sci USA* **2015**, *112*, 7650.
- [31] L. Q. Wang, L. F. Jiao, H. Yuan, J. Guo, M. Zhao, H. X. Li, Y. M. Wang, *J. Power Sources* **2006**, *162*, 1367.
- [32] J. Li, C. Cao, X. Xu, Y. Zhu, R. Yao, *J. Mater. Chem. A* **2013**, *1*, 11848.
- [33] C. M. Julien, A. Mauger, *AIMS Mater. Sci.* **2018**, *5*, 650.
- [34] K. Ku, J. Hong, H. Kim, H. Park, W. M. Seong, S. Jung, G. Yoon, K. Park, H. Kim, K. Kang, *Adv. Energy Mater.* **2018**, *8*, 1800606.
- [35] J. Hong, H. Gwon, S.-K. Jung, K. Ku, K. Kang, *J. Electrochem. Soc.* **2015**, *162*, A2447.
- [36] X. Ju, X. Hou, Z. Liu, H. Zheng, H. Huang, B. Qu, T. Wang, Q. Li, J. Li, *J. Power Sources* **2019**, *437*, 226902.
- [37] R. Baddour-Hadjean, J.-P. Pereira-Ramos, *Chem. Rev.* **2010**, *110*, 1278.
- [38] C. Julien, M. Massot, *Solid State Ionics* **2002**, *148*, 53.
- [39] B. Xu, C. R. Fell, M. Chi, Y. S. Meng, *Energy Environ. Sci.* **2011**, *4*, 2223.
- [40] Y. Huang, Y.-C. Lin, D. M. Jenkins, N. A. Chernova, Y. Chung, B. Radhakrishnan, I.-H. Chu, J. Fang, Q. Wang, F. Omenya, S. P. Ong, M. S. Whittingham, *ACS Appl. Mater. Interfaces* **2016**, *8*, 7013.
- [41] S. Venkatraman, Y. Shin, A. Manthiram, *Electrochem. Solid-State Lett.* **2002**, *6*, A9.
- [42] S.-M. Bak, E. Hu, Y. Zhou, X. Yu, S. D. Senanayake, S.-J. Cho, K.-B. Kim, K. Y. Chung, X.-Q. Yang, K.-W. Nam, *ACS Appl. Mater. Interfaces* **2014**, *6*, 22594.
- [43] Y. Qian, C. Schultz, P. Niehoff, T. Schwieters, S. Nowak, F. M. Schappacher, M. Winter, *J. Power Sources* **2016**, *332*, 60.
- [44] Y. Qian, S. Hu, X. Zou, Z. Deng, Y. Xu, Z. Cao, Y. Kang, Y. Deng, Q. Shi, K. Xu, Y. Deng, *Energy Storage Mater.* **2019**, *20*, 208.
- [45] M. Wachtler, M. R. Wagner, M. Schmied, M. Winter, J. O. Besenhard, *J. Electroanal. Chem.* **2001**, *510*, 12.
- [46] P. Niehoff, S. Passerini, M. Winter, *Langmuir* **2013**, *29*, 5806.
- [47] X. Qi, B. Blizanac, A. DuPasquier, P. Meister, T. Placke, M. Oljaca, J. Li, M. Winter, *Phys. Chem. Chem. Phys.* **2014**, *16*, 25306.
- [48] R. Dedryvère, H. Martinez, S. Leroy, D. Lemordant, F. Bonhomme, P. Biensan, D. Gonbeau, *J. Power Sources* **2007**, *174*, 462.
- [49] G. Zhuang, Y. Chen, P. N. Ross, *Langmuir* **1999**, *15*, 1470.
- [50] P. Niehoff, M. Winter, *Langmuir* **2013**, *29*, 15813.
- [51] Y. Qian, P. Niehoff, M. Börner, M. Grütze, X. Mönnighoff, P. Behrends, S. Nowak, M. Winter, F. M. Schappacher, *J. Power Sources* **2016**, *329*, 31.
- [52] J. Betz, J.-P. Brinkmann, R. Nölle, C. Lürenbaum, M. Kolek, M. C. Stan, M. Winter, T. Placke, *Adv. Energy Mater.* **2019**, *9*, 1900574.
- [53] M. Evertz, F. Horsthemke, J. Kasnatscheew, M. Börner, M. Winter, S. Nowak, *J. Power Sources* **2016**, *329*, 364.
- [54] M.-H. Ryou, Y. M. Lee, Y. Lee, M. Winter, P. Bieker, *Adv. Funct. Mater.* **2015**, *25*, 834.
- [55] J. Becking, A. Gröbmeyer, M. Kolek, U. Rodehorst, S. Schulze, M. Winter, P. Bieker, M. C. Stan, *Adv. Mater. Interfaces* **2017**, *4*, 1700166.
- [56] L. Chen, J. G. Connell, A. Nie, Z. Huang, K. R. Zavadil, K. C. Klavetter, Y. Yuan, S. Sharifi-Asl, R. Shahbazian-Yassar, J. A. Libera, A. U. Mane, J. W. Elam, *J. Mater. Chem. A* **2017**, *5*, 12297.
- [57] J. Wandt, A. Freiberg, R. Thomas, Y. Gorlin, A. Siebel, R. Jung, H. A. Gasteiger, M. Tromp, *J. Mater. Chem. A* **2016**, *4*, 18300.
- [58] G. Bieker, M. Winter, P. Bieker, *Phys. Chem. Chem. Phys.* **2015**, *17*, 8670.
- [59] S. Chen, J. Zheng, D. Mei, K. S. Han, M. H. Engelhard, W. Zhao, W. Xu, J. Liu, J.-G. Zhang, *Adv. Mater.* **2018**, *30*, 1706102.